

# Effect of Transverse Magnetic Field On Microstructure And Mechanical Properties of Ti-6Al-4V Manufactured By Laser-MIG Hybrid Welding

Chen Yue

Huazhong University of Science & Technology

Shaoning Geng (✉ [sngeng@163.com](mailto:sngeng@163.com))

Huazhong University of Science and Technology

Ping Jiang

Huazhong University of Science & Technology

Annan Yin

Huazhong University of Science & Technology

---

## Research Article

**Keywords:** External magnetic field, Laser-MIG hybrid welding, TC4 alloy, Microstructure, Mechanical properties

**Posted Date:** September 23rd, 2021

**DOI:** <https://doi.org/10.21203/rs.3.rs-913939/v1>

**License:**  This work is licensed under a Creative Commons Attribution 4.0 International License.

[Read Full License](#)

---

# Abstract

In this paper, the external transverse magnetic field is used to assist the laser-MIG hybrid welding for Ti-6Al-4V (TC4). The microstructure and mechanical properties such as microhardness and tensile properties of the weld joints under 24 mT external magnetic field (EMF) and the referring weld joint without EMF are investigated and discussed. Results show that transfer layer (TL) performs the lowest microhardness in the weld seam and tensile specimens fail in this area for the referring weld joint without EMF, which indicates the TL is the weakest zone in the weld seam. The mechanical properties of weld seam improve significantly under 24 mT EMF, which average microhardness in TL increases 9.3% and failure stress of tensile specimens improve by 16.7%, whilst a mixed fracture mode is operative in the fracture surfaces. The research reveals the elementary microstructure of TC4 laser-MIG hybrid welding is in correlation to welding heat input under the influence of EMF.

## Introduction

Ti-6Al-4V (TC4) alloy is widely applied in aerospace and astronautics due to its excellent mechanical property, high specific strength, and long service life[1, 2]. Laser-MIG hybrid welding of titanium alloys has gradually attracted the attention of researchers to improve the microstructure and the strength of welded joint in recent years[3, 4] due to its excellent combination of welding advantages of both laser welding and arc welding, such as good joint bridging performance, deep weld ability and strong weld joint strength[5].

The mechanical properties of weld joints depend on the microstructure of weld seam, especially the weakest zones such as the transition layer (TL) and heat affected zone (HAZ)[6, 7]. In general, TL indicates the changes that arise in machining structure are due to the temperature variation[8]. Wu et al. [9] indicate that high heat input and quick cooling rate during the welding process leads to the high temperature gradients and unsatisfactory microstructure. Abu et al.[10] investigate the tensile properties of TC4 for laser welding, indicate that the HAZ has poor mechanical properties. Su et al.[11] study the microstructure and tensile properties of the TC4 joint during the laser-MIG hybrid welding process, large grains, thick  $\beta$  phase, and high dislocation density caused by the high heat input leads to the low crack resistance in the whole weld seam. Thus, it is necessary to propose an effective method to assist Laser-MIG hybrid welding process, which reduces the unsatisfactory microstructure and improve mechanical property in the weakest zones.

Therefore, external magnetic field is applied to assist welding process to improve the welding structure and properties[12–19]. In laser welding, welding process will be affected when magnetic field threshold exceeds 200 mT. Chen et al.[12] have investigated the influence of 240 mT magnetic field for the laser welding of dissimilar materials. It is reported that the 240 mT magnetic field is benefit for the weld seam appearance and weld microstructure for the dissimilar materials welding. Avilov et al.[13] observe the welding bead appearance under different alternating magnetic field during the laser beam welding. It concludes that the alternating magnetic field can produce beneficial effect to inhibit gravitational drop-

out and sagging of the weld. Chen et al.[14] study the influence of magnetic field on weld appearance interfacial microstructure and mechanical properties during the high-speed GMAW,, the result shows that magnetic field can efficiently soft the weld seam, decrease the undercut defect, improve the weld mechanical properties. However, the welding process will be considerably affected when the magnetic field threshold is less than 50 mT for the arc welding. Guan et al.[15] indicate that external magnetic field (12.5 mT-17 mT) frequency had significant impact on the arc shape and arc movement, which has a considerable influence on arc temperature gradient and undercooling degree, which finally affected the weld appearance and mechanical properties in GMAW welding. Chen et al.[16] study the influence of compound magnetic field on the temperature distribution, which shows that the heat of molten pool was trended to be transmitted to the edges of weld pool under the action of compound magnetic-field. Sun et al.[17] report that the magnetic arc oscillation could result in the change of arc voltage and make the weld current flowing through sidewalls, which in turn improve the weld penetration and weld quality. Moreover, the laser-MIG hybrid welding is also profoundly influenced by the external magnetic field when the magnetic field threshold is less than 50mT. Zhang et al.[18] show that the external longitudinal magnetic field (16 mT) can increase the the stability of welding arc and affect the force on droplet transfer during the laser-MIG hybrid welding of 316L. Zhu et al.[19] indicate that combined effect of laser and magnetic field (16 mT) induces grain refinement and orientation alternation during the laser-MIG hybrid welding of 316L. It is confirmed that the appropriate magnetic field has a considerable impact on the microstructure and mechanical property during the laser-MIG hybrid welding through the literature above.

However, there is only a few systematic study on the microstructures and mechanical properties during transverse magnetic field assisted laser-MIG hybrid welding of TC4 titanium alloy. This work studies the influence of external magnetic field on the microstructures and mechanical properties in laser-MIG hybrid welding for TC4. Microstructure and properties of welded joint with the most appropriate EMF (24 mT) and that without EMF are compared in this paper, which can provide a further guidance to control the microstructure and mechanical properties of weld seam of TC4 manufactured by laser-MIG hybrid welding.

## Experimental Procedures

### 2.1 Material

In this experimental setup, TC4 base metal with the thickness of 4 mm and TC4 filled wire of 1.0 mm in diameter are adopted as the base metal and filler wire, chemical compositions of which are listed in Table 1. Physical cleaning and laser cleaning are performed on the surface of samples to eliminate the effect of surface pollution on experimental results. The pure argon with the flow rate of 2 m<sup>3</sup>/h is provided as the shielding atmosphere to protect the molten pool from oxidation.

Table 1  
Chemical composition of the base metal and the wire (wt. %)

element	Al	V	N	H	O	Fe	C	Ti
Base metal	5.5–6.8	3.5–4.5	0.05	0.015	0.20	0.30	0.10	Bal.
Weld wire	5.8	4.2	0.05	0.015	0.20	0.30	0.10	Bal.

## 2.2 Welding procedure

A 4 kW fiber laser (IPG RYL-4000) which can provide a continuous wave output with 1.07  $\mu\text{m}$  laser emission wavelength is used to weld Ti-6Al-4V plates with 4 mm by bead welding. The laser spot with a 0.3 mm diameter is focused in the center of the sheet. A Fronius TPS 4000 digital power is used as the MIG welding power controller. The transverse external magnetic field is provided by the permanent magnet blocks which can provide the maximum magnetic field of 50 mT. The sheets are put between two magnetic blocks as shown in Fig. 1. The magnetic blocks keep stationary during welding that the distribution of the magnetic induction lines is supposed to be parallel and perpendicular to the welding direction. The magnetic field intensity is adjusted by changing the distance between magnetic blocks and welded plate.

## 2.3 Mechanical testing

The Vickers microhardness on cross sections of welding bead with an interval of 0.15 mm is tested by a Vickers microhardness indentation machine at a test load of 200 g and a dwell time of 10 s. Tensile test is performed on the computer controlled electronic universal testing (CEUT) machine. Tensile specimens is cut by the wire cut electrical discharge machine and the welding bead is in the center of the tensile specimens as Fig. 2. Tensile tests are conducted on the CEUT machine with a loading rate of 2 mm/min.

## 2.4 Microstructure characterization

The analysis of the microstructure is divided into two parts: one is for the microstructural variations occurred in weld under an external magnetic field, the other is for the tensile failure tested specimen. The metallographic specimens are cut from the welded bead perpendicular to the welding direction as Fig. 2 and then are grinded by abrasive paper down to 1200 mesh size, polished by the 0.5  $\mu\text{m}$   $\text{Al}_2\text{O}_3$  slurry, chemically etched by the Kroll reagent of 2 ml HF + 6 ml  $\text{HNO}_3$  + 92 ml  $\text{H}_2\text{O}$ . The welding morphology is observed by stereoscopic optical microscope (OM) and the microstructure of metallographic specimens are characterized by the ultra depth of field OM. The detail of microstructure is captured by a SU3900 scanning electron microscope (SEM). Fractured specimens are cut from the tensile failure specimens and examined using SEM to determine the failure modes and the mechanisms of fracture initiation and propagation.

## Result

### 3.1 Weld seam morphology

Morphology of the weld seam is an important factor which indicates the weld seam bridging ability and melt metal distribution. Shapes of laser-MIG welding specimen under different external magnetic field (EMF) and the referring specimen without EMF are shown in Fig. 3. It is observed that the welding appearance is uniform with the EMF from 0 mT to 24 mT. Welding reinforcement collapse occurs under the weld process with the excessive EMF (32 mT). However, it is difficult to identify the quality of the weld bead from the weld appearance under EMF from 0 mT to 24 mT. Therefore, the influence of magnetic field on the weld microstructure and properties is necessary to study.

## 3.2 Cross-sections of the weld appearance

Figure 4 shows the cross-sections of the weld appearance under 24 mT EMF and the referring specimen without EMF. According to the thermal history undergone, the welding region can be divided into distinctive microstructural zones including the laser-arc interaction zone (LAIZ) on the top of the fusion region composed of needle-like Martensite  $\alpha'$ -grains, the laser fusion zone (LFZ) on the bottom of the fusion region composed of basketweave Widmanstätten  $\alpha'$ -grains, coarse grain in transform layer (TL) composed of coarse Widmanstätten  $\alpha'$ -grains and the fine grain heat-affected zone (FHAZ) composed of the residual  $\beta$ -grains and tiny Widmanstätten  $\alpha'$ -grains.

To investigate the influence of EMF on the microstructure distribution and analyze the characteristic of the molten pool, the dimensions of the weld region, i.e. height of the LAIZ and LFZ ( $H$ , mm), width of the TL and the FHAZ at a depth of 1 mm from the base metal surface ( $W$ , mm), reinforcement angle ( $\alpha$ , °) are measured on the cross section, which is shown in Fig. 5. For the referring specimen, the fusion zone consisted of a short LAIZ and a long LFZ, the heat-affected zone displayed the significant partition of FZ and HAZ. It can be observed that the  $H_{MZ}$  increases, the  $H_{WZ}$  decreases sharply with addition of the EMF and the main weld zone transferred from LFZ to the combination of LFZ and LAIZ. Meanwhile,  $W_{FZ}$  decreases sharply,  $\alpha$  significantly increased, width of TL decreased slightly and the form of HAZ changes from the combination of TL and FHAZ to FHAZ in dominance.

## 3.3 Metallographic structure

### 3.3.1 Macrostructure

As exhibited in Fig. 6, for the molten zone (MZ) of referring specimen without EMF, columnar primary  $\beta$ -grains nucleate at the solid-liquid interface at the edge of LAIZ and grow to the center of the molten pool against the direction of heat flow during the Laser-MIG hybrid welding process. Meanwhile, needle-like Martensite  $\alpha'$ -grains nucleate in the boundary of the columnar  $\beta$ , grow parallel from solidified columnar  $\beta$  boundary with the decrease of the temperature in LAIZ[20]. In addition, primary globular  $\beta$ -grains nucleate in LFZ,  $\alpha'$ -grains grow in the globular  $\beta$ -grains and interlaces to the basketweave Widmanstätten microstructure. For the specimen under EMF, the grains in the LAIZ are mainly primary  $\beta$ -grains that oriented from the solid-liquid interface and the growth direction is similar to that of primary  $\beta$ -grains in the LAIZ of the referring specimen. Globular  $\beta$ -grains with Widmanstätten  $\alpha'$ -grains is also observed in LFZ.

TL and HAZ of the referring specimen without EMF and the specimen under 24 mT EMF are exhibited in Fig. 7. For the referring specimen, primary globular  $\beta$ -grains nucleated at TL,  $\alpha'$ -grains grow in the globular  $\beta$ -grains and interlaced to the basketweave microstructure which is the typical Widmanstätten. Meanwhile, HAZ with fine  $\beta$ -grains are formed at low cooling rate. For the specimen under EMF, primary globular  $\beta$ -grains boundary and Widmanstätten  $\alpha'$ -grains are also observed in the TL and the boundary of TL and HAZ becomes blurred.

The average width and height of columnar  $\beta$ -grains in LAIZ and the grain size of coarse Widmanstätten in TL are specifically data analyzed to study the influence of EMF for macrostructure during TC4 laser-MIG hybrid welding, as shown in Fig. 8. Compared with the referring specimen, the width columnar  $\beta$ -grains in LAIZ under 24 mT EMF decreases from 231.7  $\mu\text{m}$  to 180.5  $\mu\text{m}$  and the height of that increases by 44.6% from 1075.5  $\mu\text{m}$  to 1555.4  $\mu\text{m}$ , while the diameter of the coarse Widmanstätten grains in TL decreases by 38.6% from 78.4  $\mu\text{m}$  to 48.1  $\mu\text{m}$ , giving rise to the increase of mechanical properties in TL.

### 3.3.2 Microstructure

The TL and HAZ microstructure of referring specimen without EMF and specimen under 24 mT EMF are depicted by SEM, while the specify observation position are marked in Fig. 4. Microstructures of HAZ for TC4 resulting from phase  $\beta$  transition mainly include residual dot-like  $\beta$ -grains, grain boundary  $\alpha_m$ , acicular Martensite  $\alpha'$ -grains and basketweave Widmanstätten structure[21]. Figure 9(a) depicts the microstructures of HAZ for referring specimen without EMF by SEM, which varied from grain to grain, generally consisting of principal basketweave Widmanstätten structure and other phase  $\beta$  transition structure with different shapes and size scales. It can be described from Fig. 9(b) that TL is composed of coarse grain basketweave Widmanstätten  $\alpha'$ -grains whose average length is 56.0  $\mu\text{m}$  and the average width is 2.4  $\mu\text{m}$  and boundary  $\alpha_m$ -grains. The primary acicular  $\alpha'$ -grains whose average length is 18.2  $\mu\text{m}$  and average width is 0.6  $\mu\text{m}$ , as displayed in Fig. 9(d). As revealed in Fig. 9(c), primary acicular  $\alpha'$ -grains nucleating from the prior  $\beta$ -grain boundary and penetrating the whole  $\beta$ -grain, intersect among themselves, constituting basketweave Widmanstätten  $\alpha'$ -grains[22]. The fine grain Widmanstätten  $\alpha'$ -grains with 18.3  $\mu\text{m}$  average length and 1.0  $\mu\text{m}$  average width and some residual dot-like  $\beta$ -grain are shown in Fig. 9(e). Figure 9(f) shows residual dot-like  $\beta$ -grain distributing between the fine grain secondary  $\alpha'$ -grains which is similar to the base metal.

Microstructure of TL and HAZ for TC4 under 24 mT EMF is also comprised by principal basketweave Widmanstätten structure and other phase  $\beta$  transition structure with different shapes and size scales as revealed in Fig. 10(a), similar to that of the referring specimen without EMF. As exhibited in Fig. 10(b), TL is composed of fine grain basketweave Widmanstätten  $\alpha'$ -grains and boundary  $\alpha_m$ -grains whose average length is 44.3  $\mu\text{m}$  and average width is 1.3  $\mu\text{m}$ , which indicates that the composition of TL is identical, nevertheless the grain boundary exhibits smaller length and width comparing with that of the referring specimen without EMF. Widmanstätten structure is composed of the intersected basketweave  $\alpha'$ -grains whose average length is 18.2  $\mu\text{m}$  and average width is 0.6  $\mu\text{m}$ , which is smaller and denser comparing with that for the referring specimen without EMF. Acicular Martensite  $\alpha'$ -grains and residual dot-like  $\beta$ -

grain are observed between the intersected basketweave  $\alpha'$ -grains respectively, as shown in Fig. 10(d). Figure 10(c) and Fig. 10(e) revealed the microstructures of HAZ, combining with the fine grain Widmanstätten  $\alpha'$ -grains whose average length is 11.6  $\mu\text{m}$  and average width is 1.5  $\mu\text{m}$  and some residual dot-like  $\beta$ -grain, exhibits smaller length and larger width comparing with that of the referring specimen without EMF. Meanwhile, magnifications of the Widmanstätten  $\alpha'$ -grains show that the tertiary  $\alpha'$ -grains are found between the secondary  $\alpha'$ -grains and residual dot-like  $\beta$ -grain distributes among them.

### 3.4 Microhardness and tensile properties

Microhardness distributions along with horizontal directions on cross sections of the referring specimen and the specimen under 24 mT EMF are marked as  $L_1$  and  $L_2$  in Fig. 4. Both weld specimens show the similar microhardness distribution trend from the base metal to the fusion zone, revealing the microhardness in fusion zone is larger than that of HAZ and base metal, low microhardness region exists in the TL and five microhardness tests of each weld specimens are tested in each conditions and the average of the results is presented as Fig. 11. Average microhardness of base metal, HAZ and MZ along with the horizontal direction for the referring specimen are 320, 375 and 420 HV respectively. And that for the TL is 310 HV, which is lower than the base metal. Those for the specimen under 24 mT EMF are 320, 370 and 400 HV respectively, which is similar to the referring specimen, however, average microhardness for the TL increases 9.3% from 320 HV to 350 HV compared with that for the referring specimen attributed to the improvement of microstructure for TL under the influence of EMF. According to Barrel Principle, improvement of the property for low microhardness region improves the strength of whole weld seam.

The weld specimens subject to tensile test failed in the TL and HAZ, whilst the transverse tensile properties of welding specimens under different EMF and base metal are shown in Fig. 12. Figure 13(a) reveals the strain-stress line of the welding specimens under different EMF and base metal, indicating that the failure stress of testing specimens improves with the increase of the EMF, meanwhile, the failure strain of testing specimens improves with the increase of the EMF from 0 mT to 24 mT and decreases under 32 mT EMF. The tensile properties of the testing specimens under 24 mT EMF are the best among the testing specimens under the EMF from 8 mT to 32 mT and the referring specimens without EMF. In each conditions two tensile experiments of each weld specimens are tested and the average of the results is presented in Fig. 13 (b). The failure strain of testing specimens improves from 12.6–15.2% with the increase of EMF from 0 mT to 24 mT. The failure stress of testing specimens improves by 16.7% from 960 MPa to 1120 MPa with the increase of EMF from 0 mT to 32 mT. Meanwhile, the failure stress of testing specimens improves by 8.3% from 960 MPa to 1040 MPa with the increase of EMF from 0 mT to 24 mT.

Figure 14 reveals tensile fractographic images of the referring specimen and the specimen under 24 mT EMF. As shown in Fig. 14 (a), fracture surface of the referring specimen without EMF is divided into two sections. Equiaxed dimples of different sizes and depths covered the area (c) of the referring specimen without EMF and the area (d) exhibited quasi-cleavage fracture characterized by cleavage surface with a wide area, demonstrating that the fracture mode of the referring specimen is mixed fracture, as shown in

Fig. 14 (c) and Fig. 14 (d). Figure 14 (b) indicates that fracture surface of the specimen under 24 mT EMF promoted the similar fraction microstructure with the referring specimen. The area (e) exhibits ductile fracture characterized by dimples with a deep depth and a large area, meanwhile, the area (f) displays quasi-cleavage fracture with a small area, demonstrating the better performance of fracture interface, as revealed in Fig. 14 (e) and Fig. 14 (f).

## Discussion

### 4.1 The influence of EMF on laser-MIG energy and molten pool

In the laser-MIG hybrid welding, the performance of the weld cross-section is mainly influenced by the heat resource, the weld pool flowing and the droplet transfer. The heat input ( $Q$ ) is mixed by the laser heat input ( $Q_{laser}$ ) and the arc heat input ( $Q_{arc}$ ).  $Q$  can be expressed by the following equation[23]:

$$Q = Q_{laser} + Q_{arc} = \frac{\eta_1 P_{laser} + \eta_2 UI}{v} \quad (1)$$

where  $P$  is the power of the laser,  $U$  is the arc voltage,  $I$  is the welding current,  $\eta_1$  is the efficiency of the laser beam,  $\eta_2$  is the efficiency of the arc power,  $v$  is the welding speed.

The arc distribution of laser-MIG hybrid welding process directly affects the efficiency of the arc power and the flow of the molten pool, ultimately affects the microstructure and performance. Arc is a strong and lasting discharge phenomenon in the gas medium between two electrodes or between electrodes and base metal with a certain voltage. The physical nature of arc is charged particles along with the current and regarded as the aggregation of electric streamline[4], which can be deeply affected by EMF. The ampere force caused by EMF on the electric streamline is backward and downward, meanwhile, The ampere force caused by EMF on the electric streamline is upward and downward. Arc is attracted by the laser in laser-MIG hybrid welding process, which leads to the predominance of forward arc. Forward arc is compressed under the filled wire by the EMF and the heat input is concentrated in the arc under the wire. Thus, heat input concentrates due to the influence of appropriate EMF. The arc voltage  $U$  and welding current are constant value, thus, the total heat input is unchanged in this process, which leads to the constant width of HAZ and penetration. The distribution of the heat is concentrated on the surface of LAIZ, which leads to the increase of LAIZ height and the decrease of LFZ height.

Electrons entering the molten pool move spirally under the influence of Lorentz force. The positive particles in the front molten pool move backward and downward under the action of EMF, which gives the molten pool in the front half a backward and downward flow; the positive particles in the tail molten pool move backward and upward under the action of EMF, which gives the molten pool in the front half a backward and upward flow. Ultimately, vertical circulation flow is produced under the influence of the transverse EMF, as shown in Fig. 15. Thus, the agitation occurs in the molten pool, which leads to the

diminution of the temperature gradient and the decrease of the cooling rate. Meanwhile, area of bottom collapse decreases under the influence of EMF.

## 4.2 Grain morphology

The grain morphology and microstructure evolution of the TC4 laser-MIG hybrid weld seam depends on the heat input of welding heat sources, the cooling rate of the weld molten pool and the distribution of temperature gradient in temperature field. The grains for TC4 have the preferential growth direction:  $\langle 10\bar{1}0 \rangle$  in HCP metal and  $\langle 100 \rangle$  in BCC metal. During the cooling process of the molten metal, the molten metal begins to solidify into a BCC structure when the temperature reaches the solid temperature, growth of the grains whose preferential growth direction is consistent with the maximum temperature gradient is accelerated and growth of the grains whose preferential growth direction is consistent with the smaller temperature gradient is inhibited[24].

For the LAIZ, heat input from laser and arc is gathering on the top of the molten pool, heat distribution decreases from the top of the molten pool to the substrate, and the primary  $\beta$ -grains tend to grow from the fusion line and the interface between LAIZ and LFZ to the top of the weld reinforcement with the shape of columnar in the in the opposite direction of the heat flow which provided the maximum driving force during solidification process[25]. The heat of molten metal mainly dissipated along the negative Z direction to the solidified  $\beta$ -grains not only from base metal by heat conduction but also at the interface between air and molten pool through convection and radiation. Consequently, the strongly directed heat flux forms from the fusion line to the top of the molten pool, generating long and narrow columnar grains penetrating the whole LAIZ[26]. Due to the high heat input and heat dissipation from the hybrid laser-MIG heat resource and the narrow molten pool width, the columnar  $\beta$ -grains are characterized as long grain length and low aspect ratio. By the influence of EMF, temperature improves in the weld center caused by the arc shrinkage, temperature gradient and cooling rate decreases due to the agitation in the molten pool. The improve of heat input in the weld center increases the height of LAIZ. For the primary  $\beta$ -grains in LAIZ, temperature gradient and cooling rate decrease improve the growth time of the columnar grains, which leads to the increase of  $\beta$ -grains boundary area. And for the LFZ, heat from the arc can hardly reach the bottom of the welding pool, which leads to the lower heat input compared with the LAIZ, eventually results in the formation of a large amount of globular  $\beta$ -grains. The grains in LFZ are hardly affected by the EMF.

## 4.3 microstructure

The microstructure of the TC4 comprised by  $\alpha$  and  $\beta$  phase possessed reversible transformation property. While the temperature of molten pool reaches the  $\beta$  transus temperature  $T_\beta$  (980°C) [20], the  $\beta$  phase transfers into  $\alpha$  phase; and when the temperature of specimen reaches martensite starting temperature  $MS$  (575°C) [27],  $\alpha$  phase transfers into  $\alpha'$  phase. During the laser-MIG hybrid welding process of TC4, the maximum temperature in the molten pool is above the liquid temperature  $T_L$  (1655°C) under the effect of the hybrid heat source, the  $\alpha$  phase transforms into  $\beta$  phase with the improve of the temperature and then melts into liquid phase when the temperature is above the liquid temperature  $T_L$  (1655°C). At the begin of

cooling, liquid phase transforms into  $\beta$  phase rapidly. With the further decrease of the temperature,  $\beta$  phase will transfer into  $\alpha$ ,  $\alpha_m$  and  $\alpha'$  phase, according to the cooling rate of the microstructure. As shown in Fig. 16, the remnant  $\alpha$  forms by the the diffusive transformation from  $\beta$  phase to  $\alpha$  phase for cooling rate between 1.5°C/s and 20°C/s, the boundary  $\alpha_m$  is obtained when the cooling rate is between 20°C/s and 410°C/s, Martensite and Widmanstatten structure composed by  $\alpha'$  transferred from  $\beta$  phase is observed when the cooling rate is above 410°C/s. For the LAIZ, acicular Martensite  $\alpha'$  and boundary  $\beta$  are observed in Fig. 6, indicating the cooling rate of the transformation process is above 410°C/s due to the high heat input under the laser-arc hybrid heat resource. However, for the LFZ, arc will hardly affect this area and laser dominants the heat resource, causing the maximum temperature and cooling rate of the LFZ decrease from MS and thus Widmanstatten  $\alpha'$  with boundary  $\alpha_m$  is easier to precipitate.

Fine grain heat-affected zone (FHAZ) is the zone the HAZ closed to base metal, composing of fine grain Widmanstatten  $\alpha'$ -grains, boundary  $\alpha_m$ -grain and residual dot-like  $\beta$ -grain. This area is far away from TL and affected by a small amount of the heat input from hybrid welding resource by heat conduction, the maximum of temperature is below the melting point, diffusive phase transition from  $\alpha$  phase to  $\beta$  phase is incomplete during the temperature-rise period, which leads to the remnant of the dot-like  $\beta$ -grain. Meanwhile, whilst the cooling rate is between 20°C/s and 410°C/s, causing transformation from  $\beta$  boundary to  $\alpha_m$  boundary and the shear transformation from  $\beta$  phase into Widmanstatten  $\alpha'$  phase. TL is the zone closed to the MZ, containing the mushy zone and the high temperature heat affected zone, causing the high cooling rate compared with that of FHAZ, and thus Widmanstatten  $\alpha'$ -grains is in the form of course grains and boundary  $\alpha_m$ -grains is also observed in TL. During laser-MIG hybrid welding, the morphological instability of dendrite is attributed to the external magnetic force calculated by welding current and magnetic field intensity[14]. As shown in Fig. 17, while the appropriate EMF (24 mT) is added into laser-MIG hybrid welding, hot metal liquid produced in the arc affected zone in molten pool prevents the primary  $\beta$ -grains growing from the high temperature heat affected zone into the mushy zone and decrease the growth time of  $\beta$  phase and Widmanstatten  $\alpha'$  phase, causing the decrease of  $\alpha'$  phase length and primary boundary  $\beta$ -grains diameter. Meanwhile, cooling rate of TL decreases, and thus diffusive phase transition from  $\alpha$  phase to  $\beta$  phase is incomplete during the temperature-rise period, which leads to remnant of the dot-like  $\beta$ -grain in TL, decrease of the Widmanstatten  $\alpha'$ -grains growth and the TL width[28]. Consequently, some residual dot-like  $\beta$ -grains and smaller Widmanstatten  $\alpha'$ -grains are observed in TL for the specimen under 24 mT EMF.

## 4.4 Mechanical properties

In addition, the higher dislocation density in martensite phase than that in  $\alpha$  phase and  $\beta$  phase could give rise to the dislocation hardening, the boundary hardening would occur while acicular  $\alpha'$ , especially the secondary and tertiary  $\alpha'$  with the smaller grain size generates[5]. Microhardness of HAZ and TL is larger than that of base metal owing to the dislocation and boundary hardening[29], and the microhardness of TL is lower than that of MZ and HAZ owing to the coarse Widmanstatten  $\alpha'$ -grains. Attributed to the finer Widmanstatten  $\alpha'$ -grains and smaller  $\alpha_m$  boundary diameters, hardness of TL increases under the influence of EMF. Tensile properties of testing specimens depend on the grain size

and dislocation conditions of the weakest zones. The solid solution strengthening of residual dot-like  $\beta$ -grains decreases dislocation density, whilst finer Widmanstätten  $\alpha'$ -grains reduce the possibility of slip bands formation, causing the improvement of tensile properties.

## Conclusions

The influence of EMF during the laser-MIG hybrid welding on morphology, microstructure, microhardness and tensile properties is investigated and discussed in this paper. The main results are summarized as follows:

- (1) With the addition of EMF, the width of the MZ and HAZ in laser-MIG hybrid welding is constant, width of TL decreases and that of HAZ increases, length of LAIZ increases and that of LFZ decreases, exhibiting obviously better formation quality than the referring specimen without EMF, attributed to the heat input concentration by the compression the forward arc and agitation occurred in the molten pool.
- (2) Heat input concentration by the compression the forward arc increase the maximum of the temperature and agitation of hot liquid flow in the molten pool decrease the cooling rate, causing increase of the columnar grains growth, which leads to the increase of  $\beta$ -grains boundary diameter in LAIZ.
- (3) Microstructure of the LAIZ consists of the columnar  $\beta$  boundary and needle-like Martensite  $\alpha'$ -grains and that of HAZ consists of the global  $\beta$ -grains boundary and Widmanstätten  $\alpha'$ -grains. The EMF increases the area of columnar  $\beta$ -grains in LAIZ and decreases the diameter of the coarse Widmanstätten grains. Microhardness of HAZ and MZ is larger than that of base metal owing to dislocation and boundary hardening.
- (4) Microstructure of HAZ consists of the Widmanstätten  $\alpha'$  phase, residual dot-like  $\beta$ -grains and grain boundary  $\alpha_m$ , whilst that of TL comprises Widmanstätten  $\alpha'$  phase and grain boundary  $\alpha_m$ . TL performs the lowest microhardness and tensile specimens fail in this zone, which indicates the TL is the weakest zone in the weld seam. For the TL, EMF decreases the coarse Widmanstätten  $\alpha'$ -grains length and the diameter of boundary  $\alpha_m$ , whilst the residual dot-like  $\beta$ -grains produce solid solution strengthening, giving rise to the increase of the tensile properties. Average microhardness for the TL increases 9.3% and failure stress of tensile specimens improve by 8.3% under 24 mT EMF compared with those of the referring specimen, while a mixed fracture mode is operative in the fracture surfaces.

## Declarations

**Funding** This research has been supported by National Natural Science Foundation of China (NSFC) under Grant No. 51861165202 and No. 51721092. The authors would also like to thank the anonymous referees for their valuable comments.

**Ethical approval** Not applicable.

**Consent to participate** Not applicable.

**Consent to publish** All the authors have reached agreement for publication.

**Competing interests** The authors declare no competing interests.

## References

1. Barui S, Panda AK, Naskar S, Kuppuraj R, Basu S, Basu B, "3D inkjet printing of biomaterials with strength reliability and cytocompatibility: Quantitative process strategy for Ti-6Al-4V,"(2019) *Biomaterials* 213: 119212. <https://doi.org/10.1016/j.surfcoat.2011.07.095>
2. Gurrappa I, "Characterization of titanium alloy Ti-6Al-4V for chemical, marine and industrial applications,"(2003) *Materials Characterization* 51: 131–139. <https://doi.org/10.1016/j.matchar.2003.10.006>
3. Huang H, Zhang P, Yan H, Liu Z, Yu Z, Wu D, Shi H, Tian Y, "Research on weld formation mechanism of laser-MIG arc hybrid welding with butt gap,"(2021) *Optics & Laser Technology* 133: <https://doi.org/10.1016/j.optlastec.2020.106530>
4. Zhu Z, Ma X, Wang C, Mi G, "Modification of droplet morphology and arc oscillation by magnetic field in laser-MIG hybrid welding,"(2020) *Optics and Lasers in Engineering* 131: <https://doi.org/10.1016/j.optlaseng.2020.106138>
5. Tang G, Chen H, Yang X, Shen L, "Effects of different welding process on the electronic temperature of plasma and weld shape during laser-MIG hybrid welding of A7N01P-T4 aluminum alloy,"(2018) *Journal of Laser Applications* 30: <https://doi.org/10.2351/1.5004434>
6. Wang W, Xu X, Ma R, Xu G, Liu W, Xing F, "The Influence of Heat Treatment Temperature on Microstructures and Mechanical Properties of Titanium Alloy Fabricated by Laser Melting Deposition,"(2020) *Materials* 13: <https://doi.org/10.3390/ma13184087>
7. Li L, Wang S, Huang W, Jin Y, "Microstructure and mechanical properties of electron beam welded TC4/TA7 dissimilar titanium alloy joint,"(2020) *Journal of Manufacturing Processes* 50: 295–304. <https://doi.org/10.1016/j.jmapro.2019.11.007>
8. Singh T, Dvivedi A, Shanu A, Dixit P, "Experimental investigations of energy channelization behavior in ultrasonic assisted electrochemical discharge machining,"(2021) *Journal of Materials Processing Technology* 293: <https://doi.org/10.1016/j.jmatprotec.2021.117084>
9. Wu M, Xin R, Wang Y, Zhou Y, Wang K, Liu Q, "Microstructure, texture and mechanical properties of commercial high-purity thick titanium plates jointed by electron beam welding,"(2016) *Materials Science and Engineering: A* 677: 50–57. <https://doi.org/10.1016/j.msea.2016.09.030>
10. Abu SHK, Cao XJ, Gholipour Baradari J, Wanjara P, Cuddy J, Birur A, Medraj M, "Determination of global and local tensile behaviours of laser welded Ti-6Al-4V alloy." pp. 859–864
11. Su X, Tao W, Chen Y, Fu J, "Microstructure and Tensile Property of the Joint of Laser-MIG Hybrid Welded Thick-Section TC4 Alloy,"(2018) *Metals* 8: <https://doi.org/10.3390/met8121002>

12. Chen R, Wang C, Jiang P, Shao X, Zhao Z, Gao Z, Yue C, "Effect of axial magnetic field in the laser beam welding of stainless steel to aluminum alloy,"(2016) *Materials & Design* 109: 146–152. <https://doi.org/10.1016/j.matdes.2016.07.064>
13. Avilov V, Fritzsche A, Bachmann M, Gumenyuk A, Rethmeier M, "Full penetration laser beam welding of thick duplex steel plates with electromagnetic weld pool support,"(2016) *Journal of Laser Applications* 28: <https://doi.org/10.2351/1.4944103>
14. Chen Q, Chen J, Lu S, Zhang Y, Wu C, "Study of high-speed GMAW assisted by compound external magnetic field,"(2020) *Welding in the World* 64: 885–901. <https://doi.org/10.1007/s40194-020-00882-7>
15. Guan ZQ, Zhang HX, Liu XG, Babkin A, Chang YL, "Effect of magnetic field frequency on the shape of GMAW welding arc and weld microstructure properties,"(2019) *Materials Research Express* 6: <https://doi.org/10.1088/2053-1591/ab2572>
16. Chen J, Chen Q, Wu C, "Study of high-speed pulsed gas metal arc welding assisted by external magnetic-field,"(2020) *Science and Technology of Welding and Joining* 25: 564–570. <https://doi.org/10.1080/13621718.2020.1774994>
17. Sun Q, Wang J, Cai C, Li Q, Feng J, "Optimization of magnetic arc oscillation system by using double magnetic pole to TIG narrow gap welding,"(2015) *The International Journal of Advanced Manufacturing Technology* 86: 761–767. <https://doi.org/10.1007/s00170-015-8214-8>
18. Zhang X, Zhao Z, Mi G, Wang C, Li R, Hu X, "Effect of external longitudinal magnetic field on arc plasma characteristics and droplet transfer during laser-MIG hybrid welding,"(2017) *The International Journal of Advanced Manufacturing Technology* 92: 2185–2195. <https://doi.org/10.1007/s00170-017-0293-2>
19. Zhengwu Z, Xiuquan M, Chunming W, Gaoyang M, "Grain refinement and orientation alternation of 10 mm 316L welds prepared by magnetic field assisted narrow gap laser-MIG hybrid welding,"(2020) *Materials Characterization* 164: <https://doi.org/10.1016/j.matchar.2020.110311>
20. Ahmed T, Rack H (1998) Phase transformations during cooling in  $\alpha + \beta$  titanium alloys. *Materials Science Engineering: A* 243:206–211. [https://doi.org/https://doi.org/10.1016/S0921-5093\(97\)00802-2](https://doi.org/https://doi.org/10.1016/S0921-5093(97)00802-2)
21. Elmer JW, Palmer TA, Babu SS, Zhang W, DebRoy T (2004) Phase transformation dynamics during welding of Ti–6Al–4V. *J Appl Phys* 95:8327–8339. <https://doi.org/10.1063/1.1737476>
22. Zeng L, Bieler TR (2005) Effects of working, heat treatment, and aging on microstructural evolution and crystallographic texture of  $\alpha$ ,  $\alpha'$ ,  $\alpha''$  and  $\beta$  phases in Ti–6Al–4V wire. *Materials Science Engineering: A* 392:403–414. <https://doi.org/10.1016/j.msea.2004.09.072>
23. Gao Z, Jiang P, Wang C, Shao X, Pang S, Zhou Q, Li X, Wang Y, "Study on droplet transfer and weld quality in laser-MIG hybrid welding of 316L stainless steel,"(2016) *The International Journal of Advanced Manufacturing Technology* 88: 483–493. <https://doi.org/10.1007/s00170-016-8774-2>
24. Brandl E, Schoberth A, Leyens C, "Morphology, microstructure, and hardness of titanium (Ti-6Al-4V) blocks deposited by wire-feed additive layer manufacturing (ALM),"(2012) *Materials Science and*

Engineering: A 532: 295–307. <https://doi.org/10.1016/j.msea.2011.10.095>

25. Brandl E, Michailov V, Viehweger B, Leyens C, “Deposition of Ti–6Al–4V using laser and wire, part I: Microstructural properties of single beads,”(2011) *Surface and Coatings Technology* 206: 1120–1129. <https://doi.org/10.1016/j.surfcoat.2011.07.095>
26. Ning J, Zhang L-J, Na S-J, Yin X-Q, Niu J, Zhang J-X, Wang H-R, “Numerical study of the effect of laser-arc distance on laser energy coupling in pulsed Nd: YAG laser/TIG hybrid welding,”(2016) *The International Journal of Advanced Manufacturing Technology* 91: 1129–1143. <https://doi.org/10.1007/s00170-016-9812-9>
27. Fu Y, Guo N, Cheng Q, Zhang D, Feng J, “In-situ formation of laser-cladded layer on Ti-6Al-4 V titanium alloy in underwater environment,”(2020) *Optics and Lasers in Engineering* 131: <https://doi.org/10.1016/j.optlaseng.2020.106104>
28. Zhang Z, Zhao Y, Shan J, Wu A, Sato YS, Tokita S, Kadoi K, Inoue H, Gu H, Tang X, “Evolution behavior of liquid film in the heat-affected zone of laser cladding non-weldable nickel-based superalloy,”(2021) *Journal of Alloys and Compounds* 863: <https://doi.org/10.1016/j.jallcom.2020.158463>
29. Yan J, Xue Y, Zhang Z, Wu Y, Zhao X, “Effect of multi-pass deformation on microstructure evolution of spark plasma sintered TC4 titanium alloy,”(2020) *High Temperature Materials and Processes* 39: 328–339. <https://doi.org/10.1515/htmp-2020-0074>

## Figures

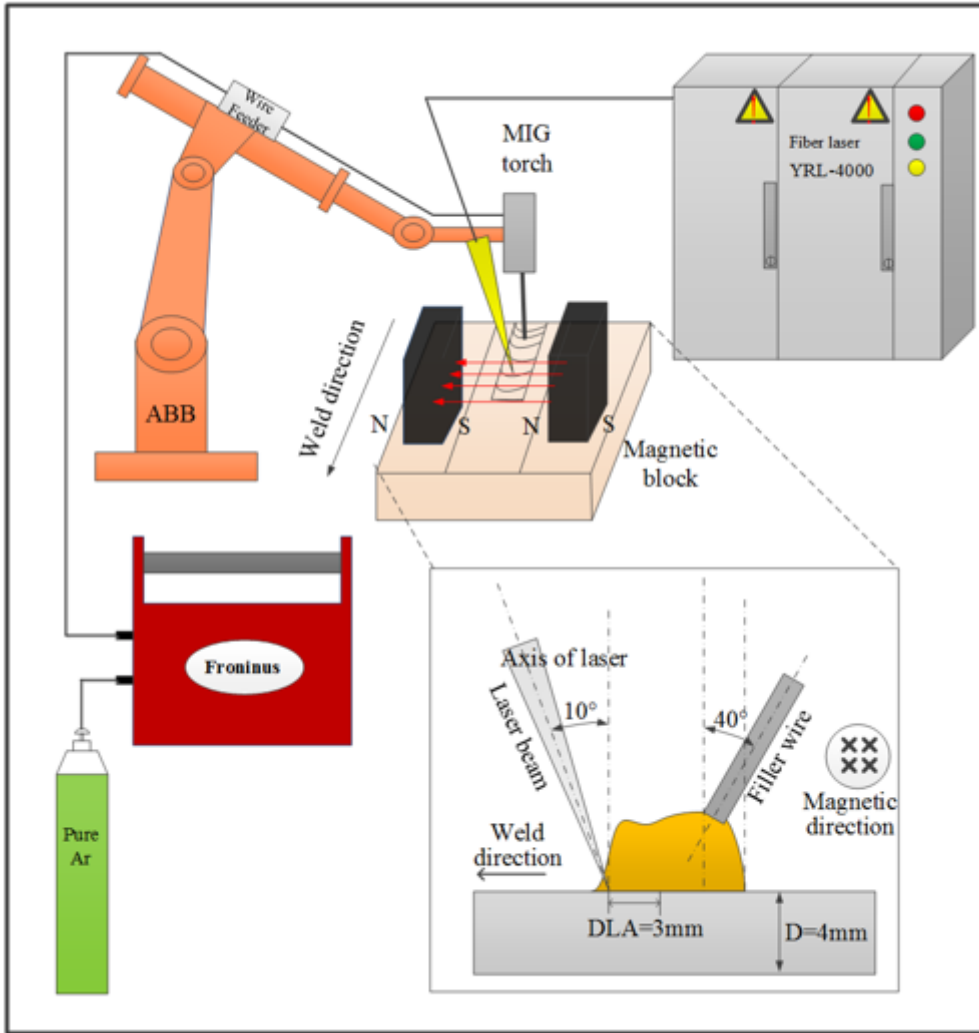


**Figure 1**

Schematic of the magnetic field assisted laser-MIG hybrid welding



**Figure 2**

Shape and size of tensile sample and metallographic specimens



**Figure 3**

Weld morphology under different EMF

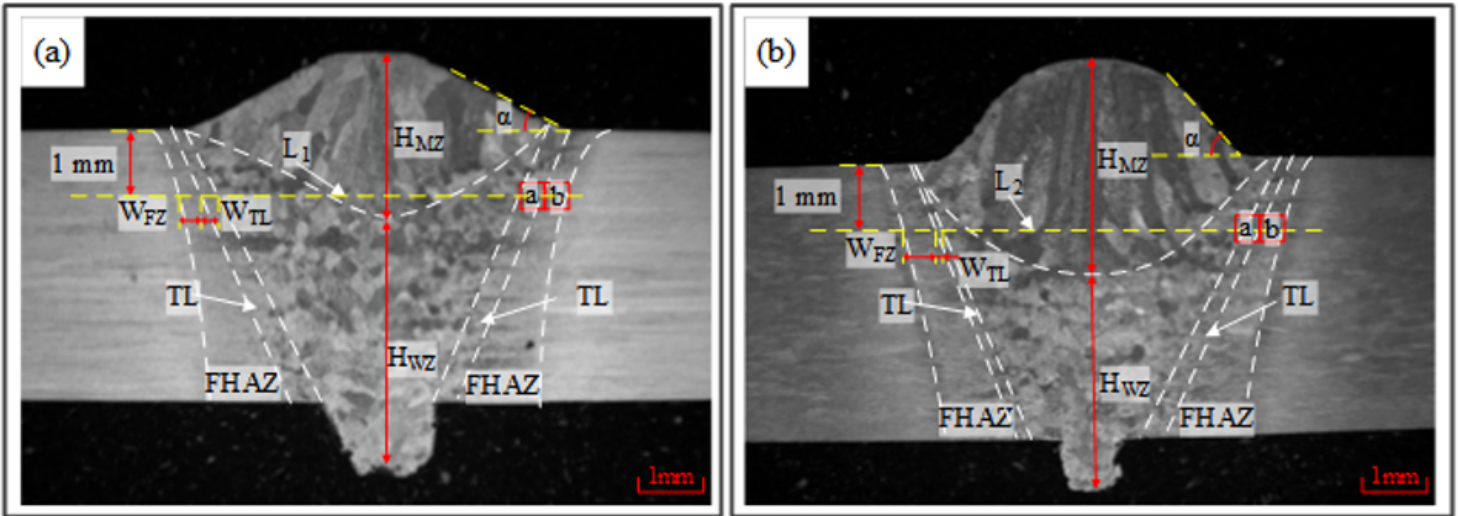


Figure 4

Influence of EMF on the microstructure distribution for weld beam (a) 0 mT (b) 24 mT

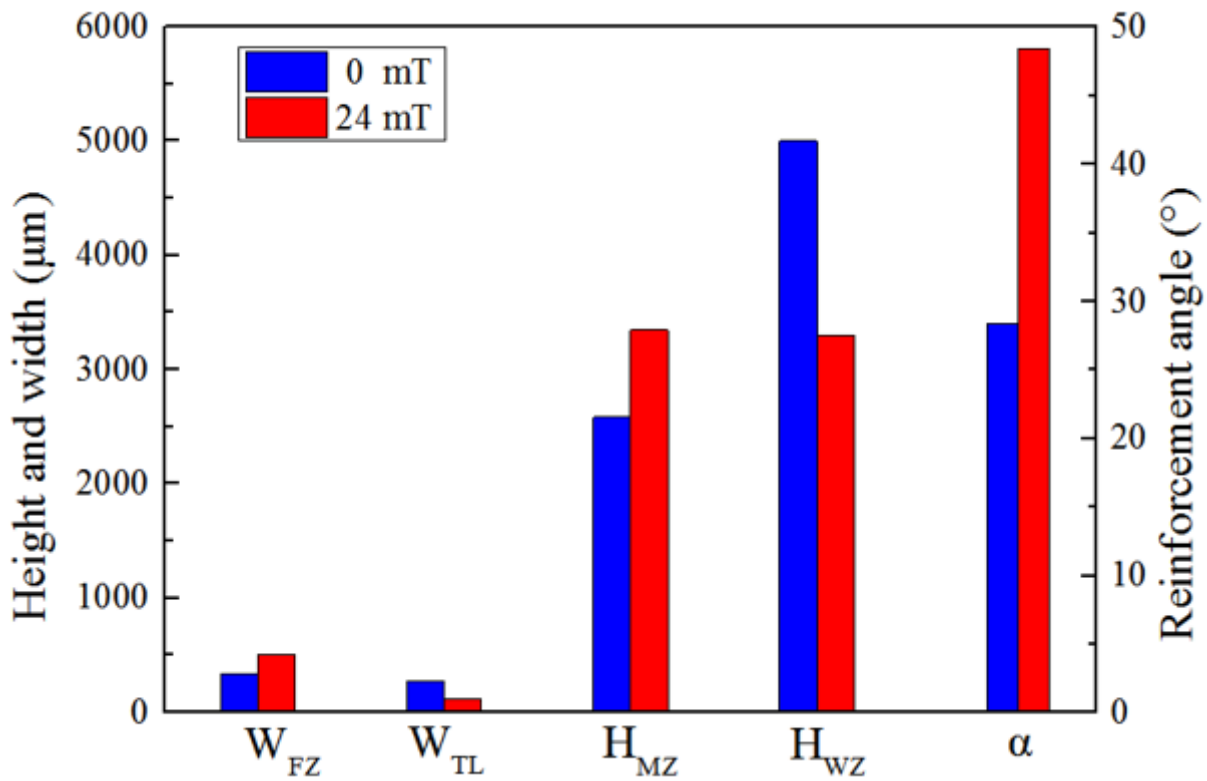


Figure 5

Weld region dimensions under 24 mT EMF and referring specimen without EMF



Figure 6

Macrostructure of molten zone under 50x OM (a) top of the referring specimen (b) bottom of the referring specimen (c) top of specimen under EMF (d) bottom of specimen under EMF



**Figure 7**

Macrostructure of TL and HAZ (a) HAZ of the referring specimen under 50x OM (b) TL of the referring specimen under 400x OM (c) HAZ of the EMF specimen under 50x OM (d) TL of the EMF specimen under 400x OM

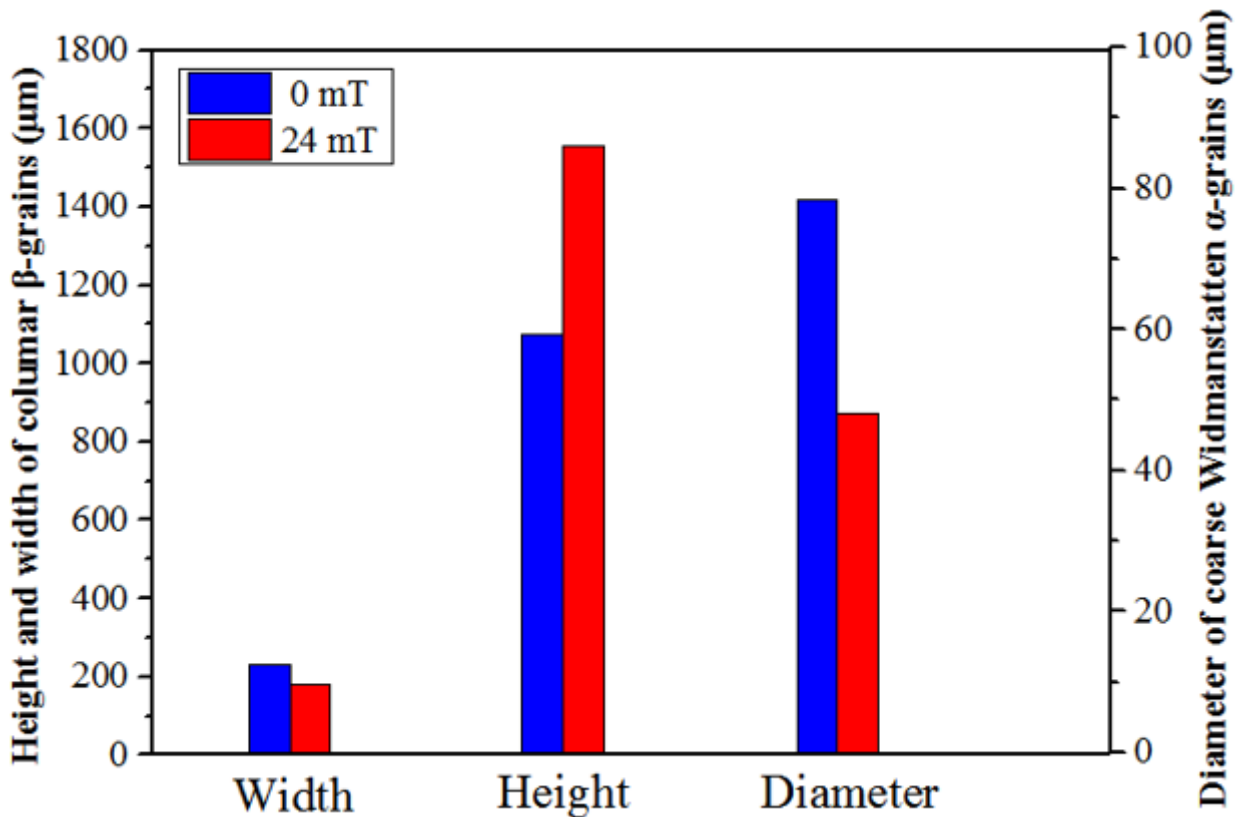


**Figure 8**

Dimensions of weld beam macrostructure under 24 mT EMF and referring specimen without EMF



**Figure 9**

Microstructure of TL and HAZ for the referring specimen (a) microstructure of zone (a) and (b) in Fig. 4(a); (b) magnifications of TL (c) magnifications of HAZ; (d) microstructure of basketweave Widmanstatten structure in TL; (e) microstructure of Widmanstatten structure in HAZ; (f) details of Widmanstatten structure and residual dot-like  $\beta$ .



**Figure 10**

Microstructure of TL and HAZ for specimen under 24 mT EMF (a) microstructure of zone (a) and (b) in Fig. 4(b); (b) magnifications of TL (c) magnifications of HAZ; (d) microstructure of basketweave Widmanstatten structure in TL; (e) microstructure of Widmanstatten structure in HAZ; (f) details of Widmanstatten structure and residual dot-like  $\beta$ .

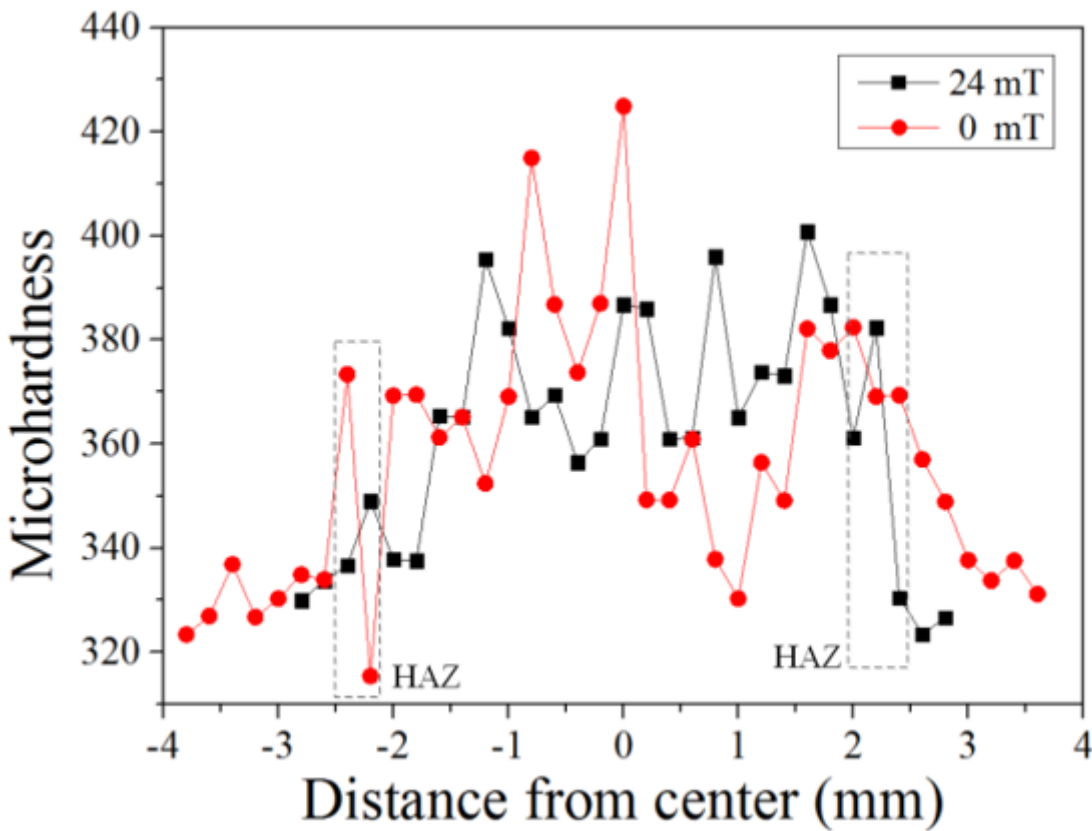


Figure 11

Microhardness distributions along with horizontal directions of the referring specimen and the specimen under 24 mT EMF



Figure 12

Crack fracture failure position under different EMF (a) 0 mT (b) 8 mT (c) 16 mT (d) 24 mT (e) 32 mT

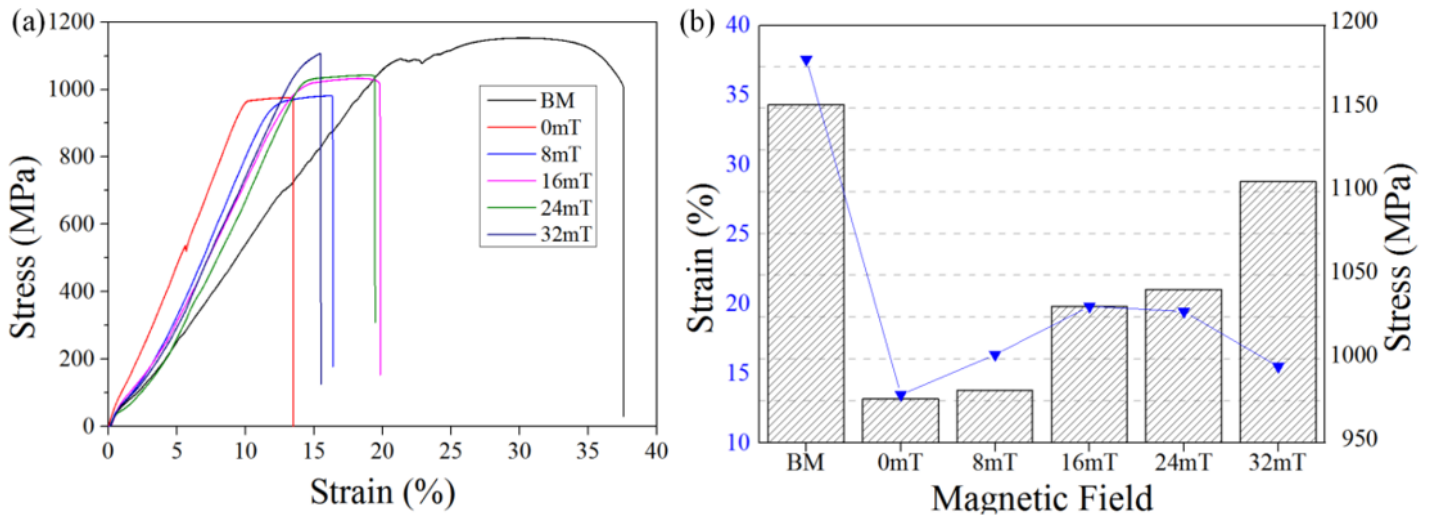


Figure 13

Tensile properties of welding specimens under different EMF and base metal



Figure 14

Tensile properties of welding specimens under different EMF and base metal

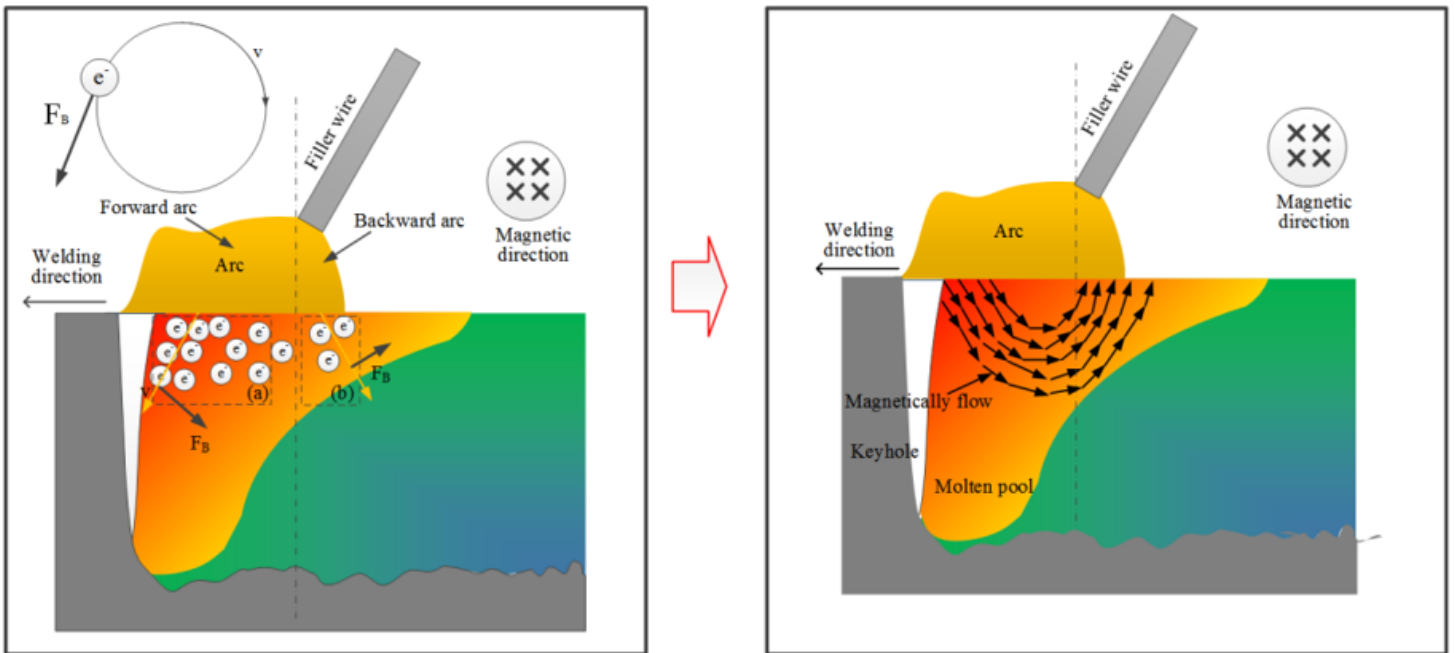


Figure 15

Effect of EMF for the molten pool during the Laser-MIG hybrid welding

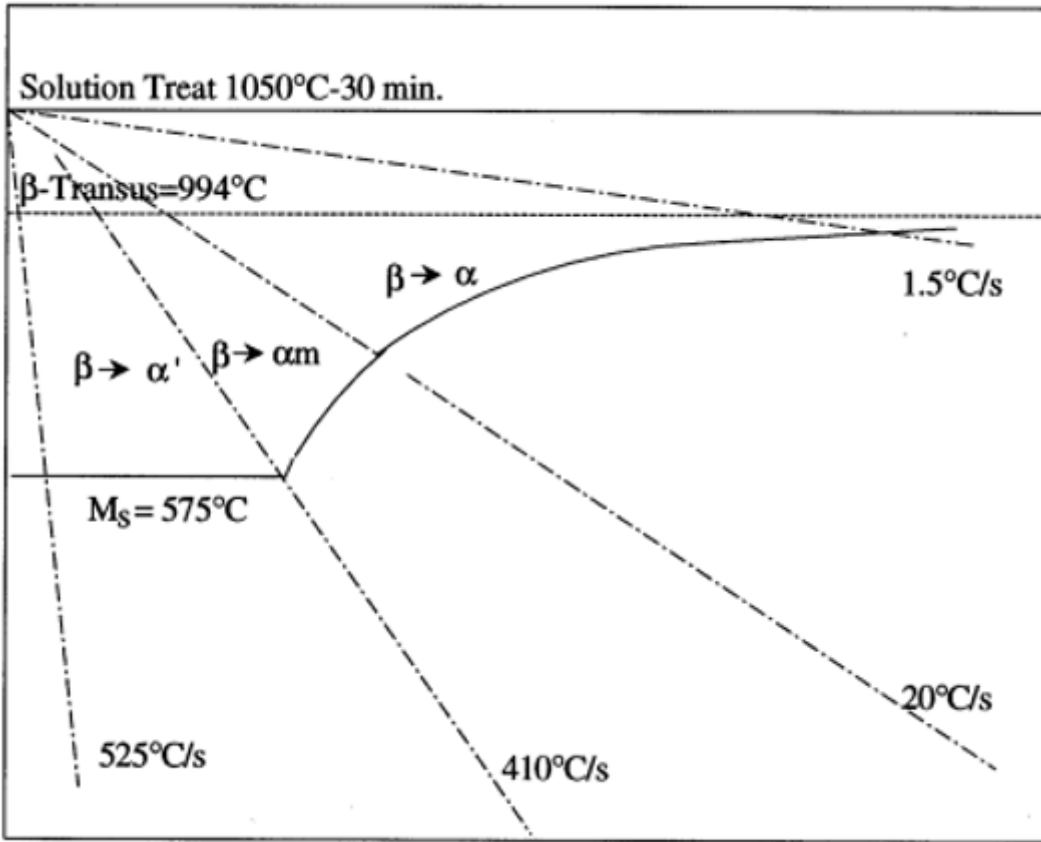


Figure 16

Schematic continuous cooling diagram for TC4  $\beta$  phase[22]

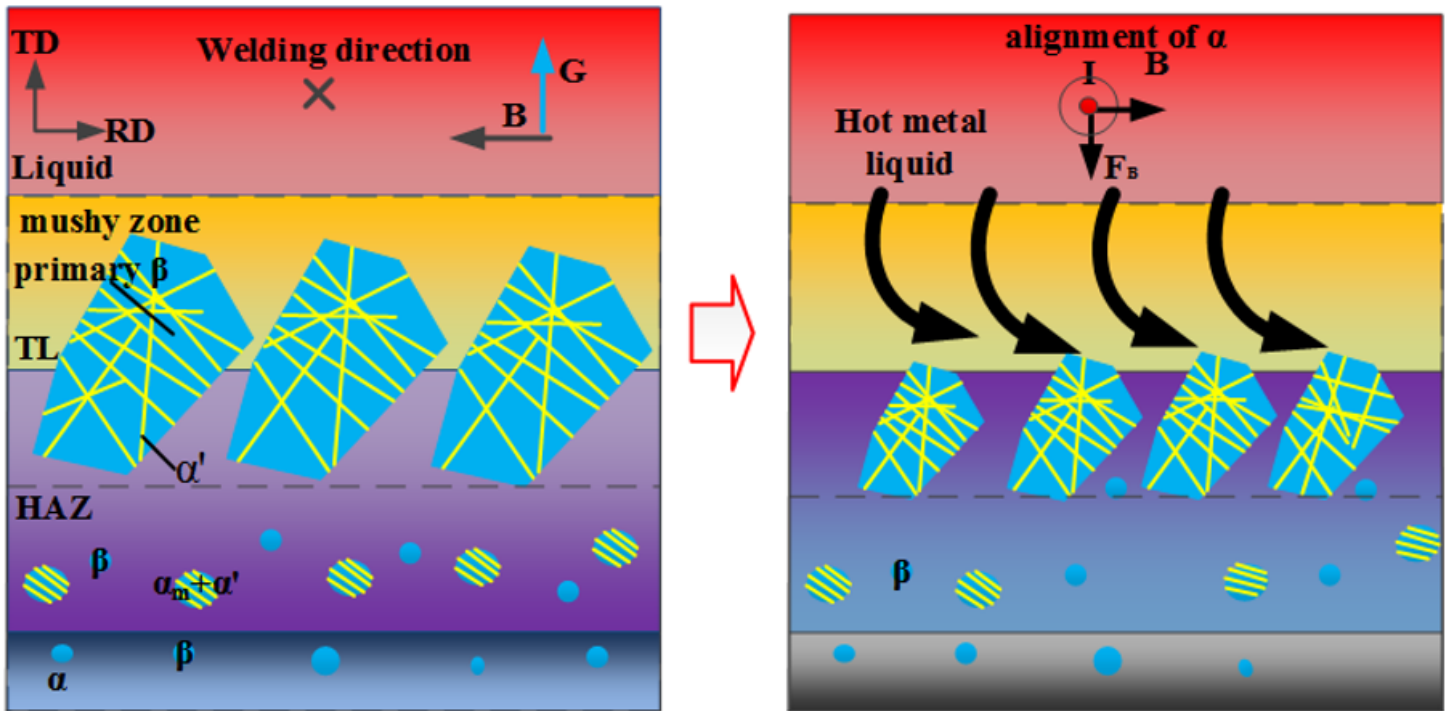


Figure 17

The influence of EMF on microstructure of HAZ